Facile MOF Support Improvement in Synergy with Light Acceleration for Efficient Nanoalloy-Catalyzed H2 Production from Formic Acid

Yue Liu, Fangyu Fu, Lionel Salmon, Bruno Espuche, Sergio Moya, Murielle Berlande, Jean-Luc Pozzo, Jean-Rene Hamon, Didier Astruc

Facile MOF Support Improvement in Synergy with Light Acceleration for Efficient Nanoalloy-Catalyzed H_2 Production from Formic Acid

Yue Liu,[a,b] Fangyu Fu,[c] Lionel Salmon,[d] Bruno Espuche,[e,f] Sergio Moya,[e] Murielle Berlande,[a] Jean-Luc Pozzo,[a] Jean-René Hamon,[b]* Didier Astruc[a]*

[a] Univ Bordeaux, ISM, UMR CNRS 5255, F-33405 Talence Cedex, France.
[b] Univ Rennes, CNRS, ISCR (Institut des Sciences Chimiques de Rennes) - UMR 6226, F-35000 Rennes, France.
[c] School of Chemistry and Chemical Engineering, Beijing Institute of Technology, Beijing, 102488, P. R. China.
[d] LCC, CNRS & University of Toulouse, 31077 Toulouse Cedex, France.
[e] Soft Matter Nanotechnology Lab, CIC biomaGUNE, Paseo Miramón 182. 20014. Donostia-San Sebastián, Gipuzkoa, Spain.
[f] POLYMAT, Applied Chemistry Department, Faculty of Chemistry, University of the Basque Country, UPV/EHU, Paseo Manuel de Lardizabal 3, Donostia-San Sebastián, 20018, Spain

E-mail: didier.astruc@u-bordeaux.fr

Abstract

Hydrogen (H_2) generation and storage are actively investigated to provide a green source of energy, and formic acid (HCOOH), a major product from the biomass, is regarded as a productive source of H_2. Therefore, improvements in heterogeneous catalysts are called for. Here, a novel type of catalyst support is proposed involving simple addition of the mixture of metal ion precursors to core-shell ZIF-8@ZIF-67 followed by reduction with $NaBH_4$, with performances surpassing those obtained using nanocatalysts in ZIF-8 or ZIF-67. The nanocatalysts Pd_xAg were optimized with ZIF-8@Pd_2Ag_1@ZIF-67 under visible light illumination for selective HCOOH dehydrogenation involving turnover frequency (TOF) value of 430 h^{-1} under light irradiation at 353 K. These results also reveal the crucial roles of the Pd sites electronically promoted in the presence of visible light by the Ag plasmon resonance and the advantageous core-shell MOF structure. In order to examine the potential extension of this catalyst improvement principle to other catalytic reactions, 4-nitrophenol reduction, a benchmarking model of catalytic reaction, was tested, and the results also confirmed the large performance superiority of ZIF-8@Pd_2Ag_1@ZIF-67 over Pd_2Ag_1@ZIF-8 and Pd_2Ag_1@ZIF-67, confirming the interest of the novel catalyst design.

Keywords: double ZIF; hydrogen production; formic acid dehydrogenation; Pd-Ag nanoalloy; plasmonic acceleration

Introduction

Hydrogen (H_2), is viewed as a key green source of energy for the close future.[1–3] Nowadays, however, only a very low percentage of H_2 is made without fossil fuel, which limits its development.[4] Formic acid (FA), with a hydrogen content of 4.4 wt %, has attracted attention a clean H_2 source.[5,6] In the course of dehydrogenation, FA decomposes to CO_2 and H_2 when a catalyst is utilized, according to Equation 1.

$$HCOOH \xrightarrow{\text{catalyst}} CO_2 + H_2 \qquad (1)$$

$\Delta G°_{298K}$ = 35 KJ mol^{-1}

Both homogeneous and heterogeneous catalysts have been applied to FA dehydrogenation,[7–12] but, in comparison with homogeneous catalysts, heterogeneous

catalysts can easily be separated and re-used.[12] Jiang et al.[13] developed a strategy using hydrophilic graphene oxide that has been reduced and N-doped (NH_2-N-rGO) as support to prepare AuPd NPs catalysts (AuPd/NH_2-N-rGO), this heterogeneous catalyst showing high capacity for dehydrogenation of FA with a turnover frequency (TOF) of 21 783 per hour at 353 K. However, with the less costly, most studied AgPd alloys, TOF values are lower. In addition, excellent performance values using GO as supports are not reproducible upon recycling with this planar support due to NP aggregation. Nevertheless, synergistic effect in bimetallic heterogeneous catalysts have often been developed as efficient catalysts for catalytic FA dehydrogenation. This is related to the increased performances obtained,[14–17] and PdAg has appeared as the most performing alloy, although the optimized compositions vary with different alloys.[18–20] Liu et al. compared catalytic performance between Pd NPs and PdAg alloys for H_2 generation using FA and highlighted the effect of synergy AgPd nanoparticles (NPs) in MOFs.[21]

The photocatalytic generation of H_2 from FA has received significant attention as an efficient dehydrogenation method to accelerate reactions.[9,22–30] Nanogold, nanosilver and nanocopper materials have often been studied for their localized surface plasmon resonance (LSPR) effect, particularly in catalysis.[31–35] Efficient sophisticated supports have been designed with complex multiple MOFs,[36] often involving ZIFs. However, the design of efficient nanocatalysts confined in two MOFs is rare, but should provide here a benefit in terms of catalytic efficiency due to improved confinement of the nanocatalyst-substrate ensemble between the two ZIFs.[36–43] Nanoparticles or nanoclusters sandwiched between two ZIFs are rare, because such nanoparticles require stabilization with polymers before organization in the nanostructure in order to avoid aggregation. In a very recent example, Lu and Yao's group disclosed ZIF-8@ZIF-67 as an excellent support of Pd-WOx nano-heterostructures[44] for FA dehydrogenation because of its hollow and large surface and number of defects at the surface providing positive interaction between Pd-WOx and ZIF-8@ZIF-67.

Inspired by the above ideas, the new type of heterogeneous catalyst, ZIF-8@PdAgNPs@ZIF-67, has been constructed. The precursor metal ion complexes are introduced in the ZIF-8@ZIF-67 composite followed by reduction with $NaBH_4$, in order to encapsulate the NP inside the outer ZIF-67 shell.

The present work also focused on an understanding of the structure-activity relationship between the composition of the PdAg NPs intercalated between the two ZIFs and their catalytic activity in FA dehydrogenation. Therefore, primarily, the catalytic activities in for FA dehydrogenation of different ZIF-8@PdAg NPs@ZIF-67 nanomaterials with various Pd and Ag proportions in their alloys has been determined and finally optimized for the Pd_2Ag NPs. Then, for this most active nanomaterial, transmission electron microscopy (TEM), high-resolution (HR) TEM including scanning transmission electron microscopy-EDS (STEM-EDS), Brunauer-Emmett-Teller (BET) equation

method, X-Ray Diffraction (XRD), X-ray Photoelectron Spectroscopy (XPS) and inductively coupled plasma optical emission spectroscopy (ICP-AES) measurements have been recorded. The catalytic performance was investigated, with the remarkable initial turnover frequency (TOF) value of 430 h^{-1} at 353 K under visible light illumination (λ = 427 nm) and high stability upon recycling five times without catalytic efficiency loss. A possible reaction pathway for FA dehydrogenation is also proposed. Finally, it was desirable to investigate whether the MOF improvement principle could be applicable to other catalytic reactions. Therefore, the rates of the standard 4-nitrophenol reduction were compared among the catalysts ZIF-8@Pd_2Ag_1@ZIF-67, Pd_2Ag_1@ZIF-8 and Pd_2Ag_1@ZIF-67, confirming superiority of the former.

Experimental methods

Materials

Potassium palladium(II) tetrachloride, sodium borohydride, formic acid, sodium formate, 2-methylimidazole, 4-nitrophenol, zinc nitrate hexahydrate and cobalt (II) nitrate hexahydrate were purchased from Sigma-Aldrich, and all of them were used without further treatment. Ultrapure water was obtained from Barnstead system for purification of water (Thermo Fisher Scientific Inc.)

Catalyst preparations

ZIF-8 : The synthesis of ZIF-8 was carried out according to a previous report.[14] Specifically, zinc nitrate hexahydrate (0.03 mol, 9.91 g) in 250 mL MeOH was poured into a solution of 2-methylimidazole (0.125 mol, 10.27 g) in 250 mL MeOH. After stirring for 1d, the product was separated by centrifugation, washed several times with MeOH and dried at 333K under vacuum for 12 h, yielding a white solid.[39]

ZIF-8@ZIF-67 : ZIF-8 (0.5 g) dispersed in 100 mL of MeOH was added into 100 mL of MeOH 2-methylimidazole (0.075 mol, 6.16 g) solution, stirred at r.t. to form solution A. Then a solution of cobalt (II) nitrate hexahydrate (0.02 mol, 5.82 g) dissolved in 100 mL of MeOH was poured into the obtained solution A under stirring. The mixture was stirred during 24 h, and the purple product was separated using centrifugation and washed 3 times with MeOH, and dried at 333K under vacuum overnight.[39]

ZIF-8@Pd_1Ag_1@ZIF-67: ZIF-8@ZIF-67 (100 mg) dispersed in 5 mL of MeOH was added to $AgNO_3$ (0.0125 mmol) and K_2PdCl_4 (0.0125 mmol dissolved in 5 mL of water. After 30 min stirring, 2 mmol $NaBH_4$[45] was added under continuous stirring, which produced ZIF-8@Pd_1Ag_1@ZIF-67 that was centrifugated and washed several times, then dried for 12 h under vacuum.

The preparations of the catalysts ZIF-8@Pd_2Ag_1@ZIF-67, ZIF-8@Pd_1Ag_2@ZIF-67, ZIF-8@Pd_4Ag_1@ZIF-67, ZIF-8@Pd_1Ag_4@ZIF-67, ZIF-8@$Pd_{16}Ag_1$@ZIF-67 and ZIF-8@Pd_1Ag_{16}@ZIF-67 were conducted following the same procedure.

Catalysis of dehydrogenation of FA by ZIF-8@PdAg@ZIF-67 in the dark

The catalytic reactions utilizing each of the nanocomposites for FA dehydrogenation were carried out in a two-necked round-bottom flask (50 mL) at 353K under ambient atmosphere. Specifically, 75 mg of as-prepared catalyst was kept in the flask with 2 mL water, and the catalytic reaction started immediately after adding a solution containing FA (3 mmol) and sodium formate (SF, 1 mmol). The gas volume generated was recorded from the change of the water level in the burette.

Catalysis of dehydrogenation of FA by ZIF-8@PdAg@ZIF-67 under visible-light illumination

The reactions under light were carried out by using the photocatalytic equipment PR160L, LED PhotoReaction Lighting (Kessil lighting company, USA). The LED-type lamps were switched on during 15 min before visible light illumination in order to make sure that the intensity of the light is stable. The decomposition of FA catalyzed by PdAg@ZIF-8@ZIF-67 was followed using the method mentioned above. The intensity of the irradiated light was adjusted switched from10 W to 40 W, including the intensity 25% (10 W), 50% (20 W), 75% (30 W) and 100% (40 W), respectively.

NaOH trap test

To investigate the gas composition and the molar ratio of CO_2 and H_2 generated from the ZIF-8@PdAg@ZIF-67 catalyzed dehydrogenation of FA, a two-necked round-bottom flask (50 mL) containing 5 M NaOH solution as a NaOH trap was connected between the reaction flask and the gas burette.

Recyclability test

For the recyclability test, the catalyst was separated after dehydrogenation using centrifugation and washing with distilled water three times. Then, the catalyst was re-dispersed in a two-necked round-bottom flask (50 mL), and the same experimental operation was carried out for five cycles.

Results and discussion

Nanocatalysts synthesis and characterization

FA dehydrogenation was conducted using bimetallic nanomaterials prepared, via a typical wet chemical reduction approach, using prepared ZIF-8@ZIF-67 in MeOH and the metal salt using the following Pd/Ag ratios : 1:1, 1:2, 1:4, 1:16, 16:1, 4:1, 2:1 dissolved in water, followed by fast reduction of the metal ions at r.t. with an aqueous solution of sodium borohydride. [46] The metal contents of the nanocatalysts were quantified by ICP-AES measurement (Table S1). The catalytic dehydrogenation of FA was performed in the dark with all the catalysts at 353 K including SF (n_{FA} = 1 mmol, n_{SF} = 3 mmol, Figure 1), and the catalytic activity varied as a function of the ratio of metals. The nanomaterial ZIF-8@Ag@ZIF-67 had almost no catalytic activity, whereas together with Pd in alloys, the catalytic activity increased together with Pd content. ZIF-8@Pd_2Ag_1@ZIF-67 was the most active alloy catalyst for FA dehydrogenation, showing a $TOF_{initial}$ value of 245. With further increasing the Pd proportion in Pd_xAg until pure ZIF-8@Pd@ZIF-67, the alloy catalyst became less active, highlighting the optimization of the synergy effect in the Pd_2Ag alloy composition in ZIF-8@ZIF-67. Compared with Pd_2Ag_1@ZIF-8 and Pd_2Ag_1@ZIF-67 in dark condition (Figure 2a) and under light irradiation (Figure 2b), the nanocatalyst immobilized between the two ZIF layers exhibited higher catalytic performances than the same amount of Pd_2Ag_1 NPs immobilized inside ZIF-8 or ZIF-67, which is attributed to the specific sandwich structure of ZIF-8@ZIF-67 and reaction confinement herein. This is already true in the dark, but is even more marked under visible-light illumination, showing the importance of inter-ZIF confinement synergies. Furthermore, the TOF comparison with those obtained with other supports (Table S2), such as TiO_2 [36] and carbon materials [17] shows that the catalytic activity of PdAg NPs immobilized on ZIF-8@ZIF-67 is very competitive and enhances the synergistic effect among the two metals of PdAg alloy by interaction with ZIF-8@ZIF-67.

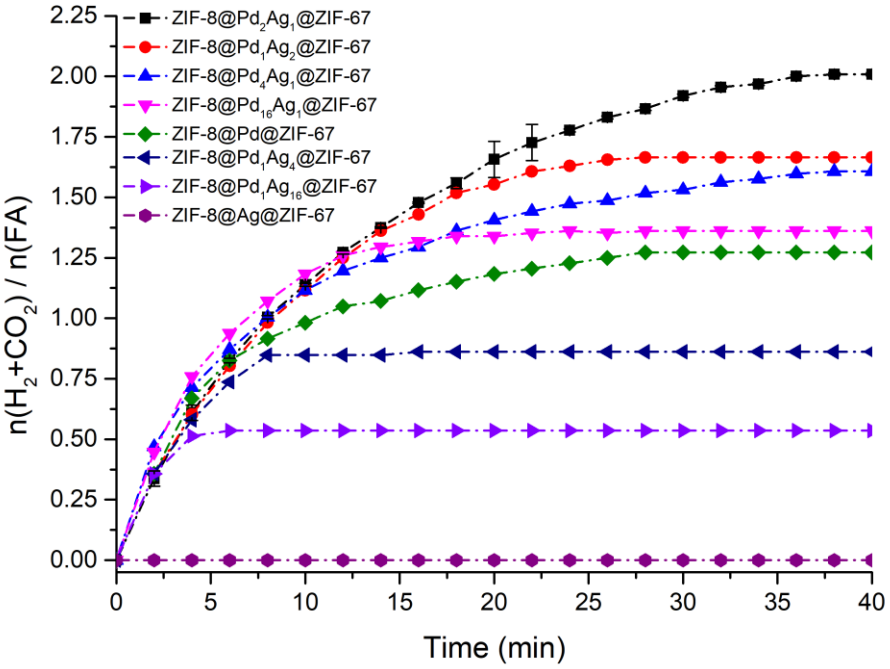

Figure 1. Gas generation for FA dehydrogenation with different ratios of Pd/Ag supported on ZIF-8@ZIF-67 versus time at 353K in dark.

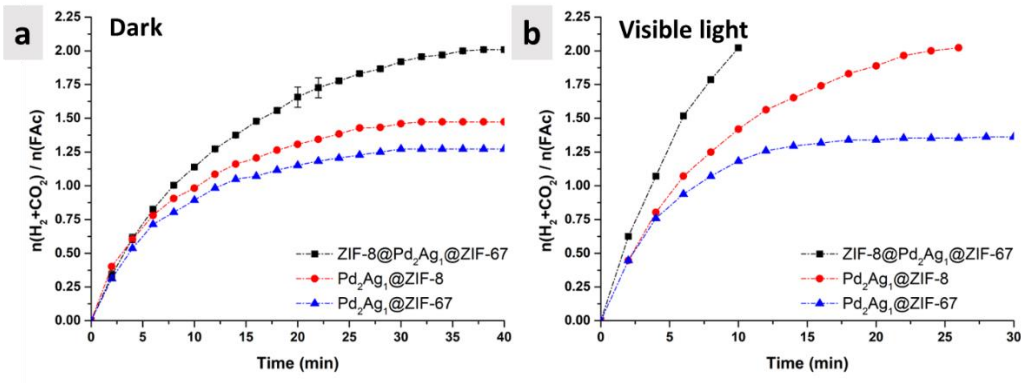

Figure 2. Gas generation for FA dehydrogenation supported on Pd_2Ag_1@ZIF-8, Pd_2Ag_1@ZIF-67 and ZIF-8@Pd_2Ag_1@ZIF-67 vs. time at 353K(a) in the dark, (b) under visible light.

Following this optimization of the proportion of the two metals in their AgPd alloys in ZIF-8@ZIF-67, the typical morphology and structure of the ZIF-8@Pd_2Ag_1@ZIF-67 were characterized by TEM and HRTEM images (Figure 3a, b). As shown in Figure 3a, the nanocatalyst is composed of all nearly spherical particles with good dispersity without any agglomeration, and their mean diameter in the interlayer of ZIF-8@ZIF-67 is about 2.4 nm (insert in Figure 3a). Additionally, the HRTEM results (Figure 3b)

reveal that the (111) lattice fringe distance of *in situ* synthesized face-centered cubic (*fcc*) PdAg alloy is 0.23 nm, between the (111) lattice spacing of *fcc* Ag (0.24 nm) and *fcc* Pd (0.22 nm).[47] The ZIF-8@Pd_2Ag_1@ZIF-67 was further characterized by HAADF-STEM image and STEM-EDS mapping (Figure 3c-g). Elemental mapping of the ZIF-8@Pd_2Ag_1@ZIF-67 reveal a typical core-shell structure: the Zn element is mainly located inside, while the Co element is mainly dispersed in the shell part.

The XRD study was carried out in order to investigate the ZIF-8@Pd_2Ag_1@ZIF-67 crystalline structure. As shown in Figure S1, sharp peaks at 7.4° and 12.8°, indicate that the constructed core shell structure is highly crystalline.[41] Diffraction peaks for Pd (111) (JCPDS No. 87-0643) at 40.1° and 46.6° are shown in ZIF-8@Pd_2Ag_1@ZIF-67. There are characteristic peaks of Ag in the XRD pattern because of its low loading content (0.8 wt% as shown in table S1) and the small size at the surface of the catalyst (Figure 3a), similarly to previous literature results.[48–51]

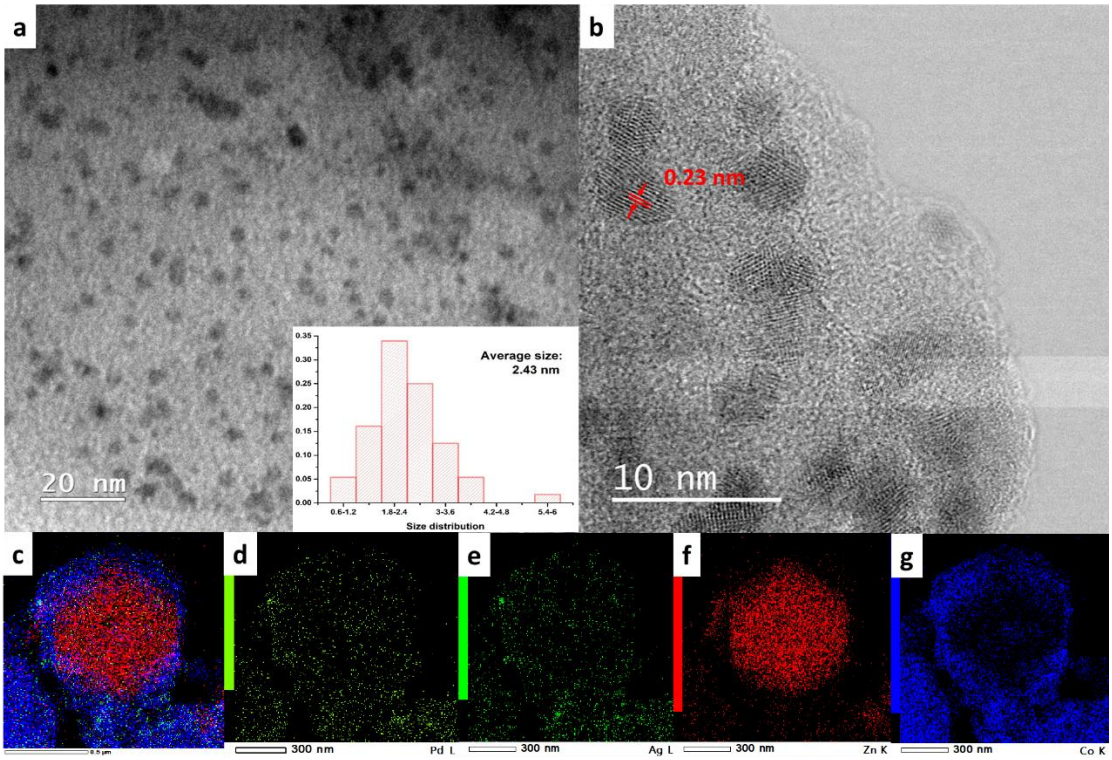

Figure 3. TEM image (a), HRTEM image (b), combined elemental mapping (c), Pd (d), Ag(e), Zn (f) and Co (g) compositional mapping of ZIF-8@Pd_2Ag_1@ZIF-67.

The specific Brunauer-Emmet-Teller (BET) surface area and pore distribution of the parent ZIF-8, ZIF-8@ZIF-67 and ZIF-8@Pd_2Ag_1@ZIF-67 were found using N_2 adsorption-desorption isothermal measurements. All isotherms pertain to type-I isotherm and high N_2 absorption at 77k, indicating the presence of a hollow metal-organic frameworks architecture with high porosity (Figure S2-S4). The distribution of pore sizes and total volume of the pores of the samples were determined by density

functional theory (DFT) and Saito-Foley (SF) (Figure S2-S4 and Table 1). The pore diameter of the ZIF-8@ZIF-67 (1.75 nm) gradually increased compared to that of ZIF-8 itself (1.39 nm), and the BET surface area of the ZIF-8@ZIF-67 (2160.8 $m^2 g^{-1}$) shows increase compared to ZIF-8 itself (1857.9 $m^2 g^{-1}$). This increment is attributed to the size increase of the shell of ZIF-67 on the surface of ZIF-8 itself without blockage of the pores at the core-shell interfaces.[41,51,52] After the addition of PdAg NPs, the surface and total volume of the pores of ZIF-8@ZIF-67 indicated a decrease, which suggests that the core-shell ZIF pores are occupied by PdAg NPs, which is consistent with the HRTEM results (Figure 3).

Table 1. Physical Properties of the nanocatalysts on ZIF-8.

Sample	BET surface area ($m^2 \cdot g^{-1}$)	Average Pore Diameter (nm)	Pore volume ($cm^3 \cdot g^{-1}$)
ZIF-8	1,857.9	1.39	0.6456
ZIF-8@ZIF-67	2,160.8	1.75	0.9478
ZIF-8@Pd_2Ag_1@ZIF-67	1,287.56	1.9	0.6116

Kinetic studies of ZIF-8@Pd2Ag1@ZIF-67 in the FA dehydrogenation reaction and comparison with Pd2Ag1@zif-8 and Pd2Ag1@ZIF-67

The kinetic trends of the performances of ZIF-8@Pd_2Ag_1@ZIF-67 in the FA dehydrogenation reaction were evaluated at various concentrations of SF in the 1-4 mmol range (Figure 4a) and in the temperature range of 313-353 K (Figure 4b). In order to explore the best concentration of SF, solutions with various molar ratios of FA and SF (1:1, 1:2, 1:3, and 1:4) were made toward FA dehydrogenation. The gas collected exhibits an increasing-decreasing shape, the highest gas generation being observed when the molar ratio FA/SF was 1: 3. Additional increase of the amount of SF resulted in the decrease of gas generation, which is assigned to a too high anion density ([$HCOO^-$]) saturating the nanocatalyst surface, which inhibits substrate activation by the surface Pd atoms. The data of the time dependence of H_2 formation catalyzed by ZIF-8@Pd_2Ag_1@ZIF-67 at various temperatures is indicated in Figure 4b. According to the Arrhenius equation, the activation energy (*E*a) of FA dehydrogenation is 19.6 ± 1.3 kJ/mol (Figure S5). The highest gas generation was observed when the temperature was 353 K. Based on these experimental results, the optimized temperature further used was fixed at 353 K with the optimized molar ratio of FA/ SF, 1:3.

The stability and recyclability of the heterogeneous catalyst are playing a key role in industrial applications. Thus, the recycling experiments of ZIF-8@Pd_2Ag_1@ZIF-67 were carried out for the dehydrogenation of FA at 353 K, the DATA being gathered in Figure 4c. The catalytic activity of ZIF-8@Pd_2Ag_1@ZIF-67 remained almost the same as that of the initial catalyst in H_2 generation, exhibiting no significant decrease even after five recycling runs. The reason for which the gas amount generated in the fifth run was a little less than that of the fourth run, as already reported for other PdAg catalysts,[21,53,54] probably is a low amount of PdAg NP aggregation.

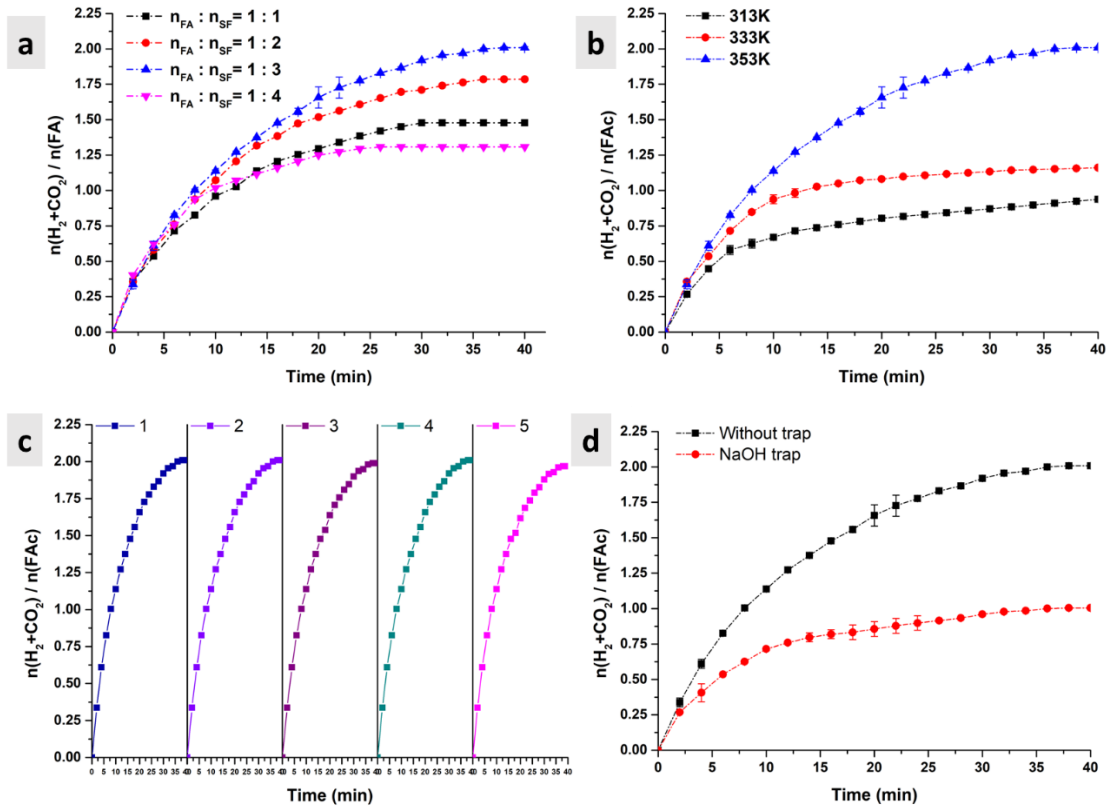

Figure 4. Plots of the gas generation vs. time for FA dehydrogenation catalyzed by ZIF-8@Pd_2Ag_1@ZIF-67 (a) with various ratios of FA/SF; (b) at different temperature; (c) recyclability; (d) with and without NaOH trap (for CO_2 gas).

The gas generated from the dehydrogenation of FA catalyzed by ZIF-8@Pd_2Ag_1@ZIF-67 was passed through a 5 M NaOH trap in order to investigate the gas composition and the CO_2 / H_2 molar ratio. The volume of gas was reduced to half with the NaOH trap, confirming the full absorption of CO_2 and, importantly, the absence of CO (Figure 4d). The of CO_2/H_2 molar ratio in the gas generated is 1:1, confirming the stoichiometry of FA dehydrogenation in Equation 1.

Visible-light-induced acceleration of ZIF-8@Pd_2Ag_1@ZIF-67-catalyzed FA dehydrogenation

There have been very few reports on the visible-light-driven dehydrogenation of FA into H_2 using MOFs as catalysts, to date.[55–57] The photocatalytic performance of ZIF-8@Pd_2Ag_1@ZIF-67 for the dehydrogenation of FA was tested under visible-light irradiation with various wavelengths (Figure 5a) and different intensities (Figure 5b). As shown in Figure 5a, the light source of λ = 527 nm was ineffective, as the amount of gas generated from FA dehydrogenation utilizing this wavelength of light was identical to that for the reaction without light irradiation. On the other hand, the light sources of λ = 370 nm and λ = 427 nm enhanced the dehydrogenation of FA, which signifies that the visible light is only efficient in the PdAg plasmonic domain. This confirms that it is the Ag plasmon excitation that boosts catalysis. Indeed, the UV-Vis. absorption spectrum of ZIF-8@Pd_2Ag_1@ZIF-67 is broad between 350 and 500 nm. A large enhancement was observed with λ = 427 nm light illumination, approaching the maximum of the plasmon wavelength (λ = 402 nm) for this nanocatalyst, the plasmon band intensity at 427 nm being close to the maximum at 402 nm (Figure S6).[58] Additionally, the effect of light intensity at λ = 427 nm on the photocatalytic dehydrogenation of FA catalyzed by ZIF-8@Pd_2Ag_1@ZIF-67 was examined (Figure 5b), and the rate of H_2 generation increased in the same time as that of light intensity. This indicates that the catalyst activity of ZIF-8@Pd_2Ag_1@ZIF-67 was easily controlled by the light intensity. These wavelength and intensity dependencies clearly confirm the positive role of the plasmon influence in boosting the catalytic performance and demonstrate the great promise of the ZIF-8@Pd_2Ag_1@ZIF-67 as a more efficient photocatalyst for H_2 generation from FA. The contribution of photo thermalization induced by plasmon photons[59–61] has been analyzed. The flask was covered with tin paper in order to inhibit direct visible light illumination, and a temperature probe was located inside the vessel that contained the reaction mixture to monitor the change of temperature during H_2 generation from FA catalyzed by ZIF-8@Pd_2Ag_1@ZIF-67. The temperature changed within 2 °C was observed during the maximum reaction time (Figure S7a) and there was no significant change of gas generation between catalyzed by ZIF-8@Pd_2Ag_1@ZIF-67 with tin paper covered and in dark (Figure S7b). Thus, photothermalization is not the main responsible factor for the light-induced catalytic activity enhancement[62,63] of the catalyzed FA dehydrogenation reaction.

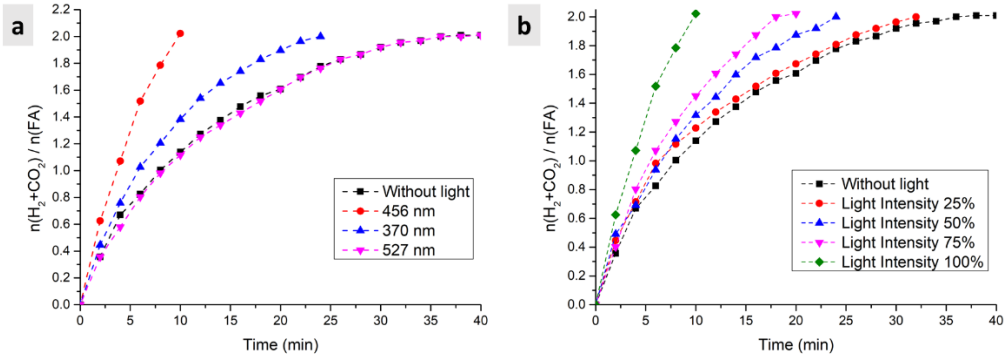

Figure 5. Plots of the gas generation vs. time for H_2 generation from FA catalyzed by ZIF-8@Pd_2Ag_1@ZIF-67 under visible-light irradiation (a) with various wavelengths, (b) with various light intensities.

The promotional role of the plasmonic effect was verified by XPS measurements (Figure 6) in order to investigate the surface chemical compositions and valence states before and after reaction under light. As a result, a possible mechanism for visible light-enhanced FA dehydrogenation catalyzed by ZIF-8@Pd_2Ag_1@ZIF-67 is proposed in Scheme.1. First, SF coordinates onto the catalytic metal surface, transferring its negative charge onto the alloy. This increases the ability of the metal surface to carry out oxidative addition of the H--COOH bond, forming the intermediates HCOO* and H* that serve as ligands on the metal surface. On the alloy surface, the coordinated HCOO* group may be in equilibrium between its monohapto (κ^1-OC(O)H) and dihapto chelate (κ^2-O_2CH) forms. However, the more flexible monohapto form is privileged toward further β-elimination step giving the second hydride ligand H* on the metal surface while CO_2 escapes from the surface. The last step, involving reductive elimination of the two surface ligands H* to give H_2, is known to be accelerated by visible-light irradiation.[64-67] The light illumination provokes plasmonic "hot" electron transfer from an Ag atom to a Pd atom of the alloy surface,[55] which increases its electron density, favoring both the β-elimination and reductive elimination steps. In sum, both SF anion coordination and plasmonic "hot" electron transfer from Ag are enriching the electronic state of Pd that is responsible for the key reaction steps. Combined with XPS results in Figure 6, the binding energy of Ag 3d at 376.23 and 370.23 eV before reaction moved after the reaction to higher values (376.78 and 370.61 eV) (Figure 6a), showing that the Ag atoms became charged more positively. In the same time, the Pd 3d (343.86 and 338.38 eV) signals moved to lower values (343.20 and 337.89 eV) after reaction (Figure 6b), demonstrating that there was an electronic stimulation following the photoreaction. This high-energy plasmon-excited electron transferred from Ag to Pd, resulting from a heterogeneity of charge at the interface between Ag and Pd, results in the electronic enrichment of the nearby Pd atom.[68,69]

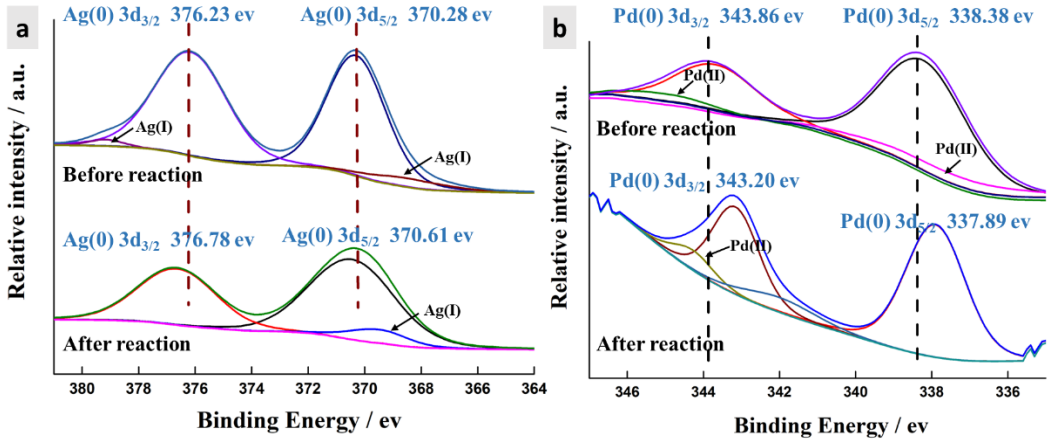

Figure 6. XPS spectra of ZIF-8@Pd_2Ag_1@ZIF-67, (a) Ag region before and after reaction, (b) Pd region before and after reaction.

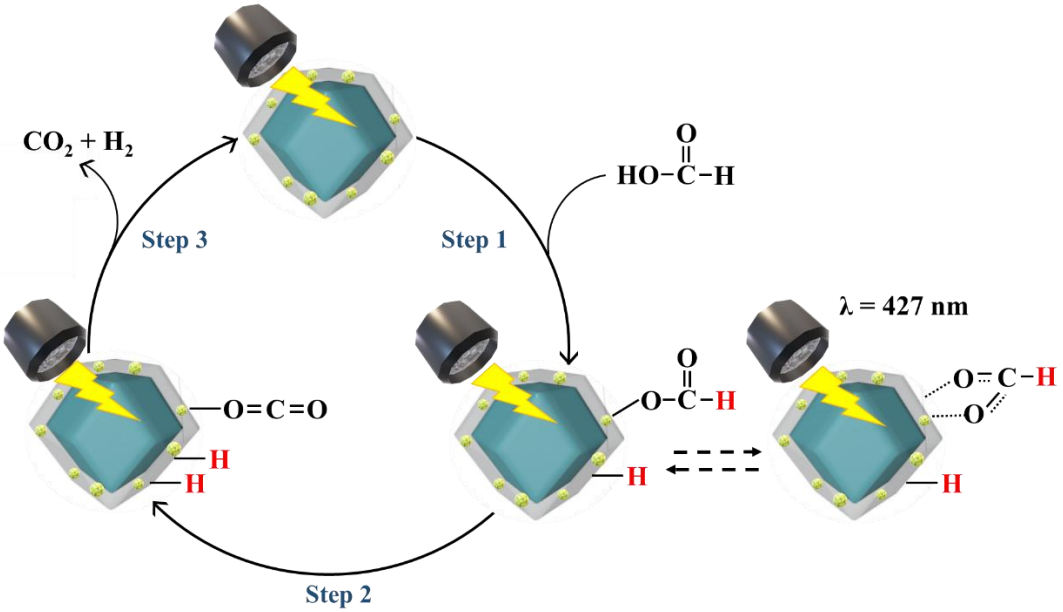

Scheme 1. Proposed reaction pathway for visible light-enhanced H_2 generation from FA catalyzed by ZIF-8@Pd_2Ag_1@ZIF-67.

Comparison of the catalytic performances of ZIF-8@Pd2Ag1@ZIF-67, Pd2Ag1@ZIF-8 and Pd2Ag1@ZIF-67 in 4-nitrophenol reduction by $NaBH_4$.

The catalyst activities of the new nanocatalysts were examined upon reduction of 4-nitrophenol (4-NP)[70,71] with $NaBH_4$ at 22 °C. Typically, the experimental solution was prepared by mixing 9 ml of freshly prepared aqueous $NaBH_4$ (75 mg, 2 mmol) solution with 12 ml of aqueous 4-NP solution (3 mg, 0.02 mmol). Subsequently, 3.5 mg of catalyst was dispersed in 0.1 or 1.0 ? ml methanol and sonicated during 3 min. After sonication, the 0.1 or 1.0 ? ml of methanol solution containing the catalyst was added to the experimental solution, and the yellow solution gradually became colorless. UV–Vis. spectroscopy monitored the catalytic reaction progress between 250 and

550 nm. The absorbance change at 400 nm allowed to calculate the rate constant of the reaction.

The course of the reaction was checked using the kinetics utilizing UV–Vis. spectroscopy at various intervals of time (Figure 7). The color of ZIF NPs catalysts (figure 7a) is white for Pd_2Ag_1@ZIF-8, deep purple for Pd_2Ag_1@ZIF-67, and light purple for ZIF-8@Pd_2Ag_1@ZIF-67. The absorption band at 400 nm only presented a slight decrease after 30 min without catalyst (Figure 7b). In the presence of catalyst, the reduction immediately started upon stirring, induction time (figure 7c-e). The band located at 400 nm corresponding to 4-NP absorption rapidly decreased. The plot of the consumption rate of 4-NP [$-\ln (C/C_0)$] vs. reaction time provides the apparent rate constant k_{app} (figure 7f). The reactions catalyzed by the different catalysts ZIF-8@Pd_xAg_y@ZIF-67 were all finished with 100% conversion within 4 minutes, showing the efficiency of all these nanocatalysts, ZIF-8@Pd_2Ag_1@ZIF-67 possessing the best catalytic ability.

Table S3 shows the comparison of the apparent rate constants for 4-NP reduction with other transition metal NPs from the literature. In comparison with the three ZIF NPs catalysts in our work, ZIF-8@Pd_2Ag_1@ZIF-67 has the highest k_{app} value in the reduction of 4-NP by $NaBH_4$. Compared to Au, Rh and α-Fe_2O_3 nanoparticles in the Table S3, ZIF-8@Pd_2Ag_1@ZIF-67 is the best, most active catalyst for 4-NP reduction with k_{app} of 1.8×10^{-2} s^{-1}.

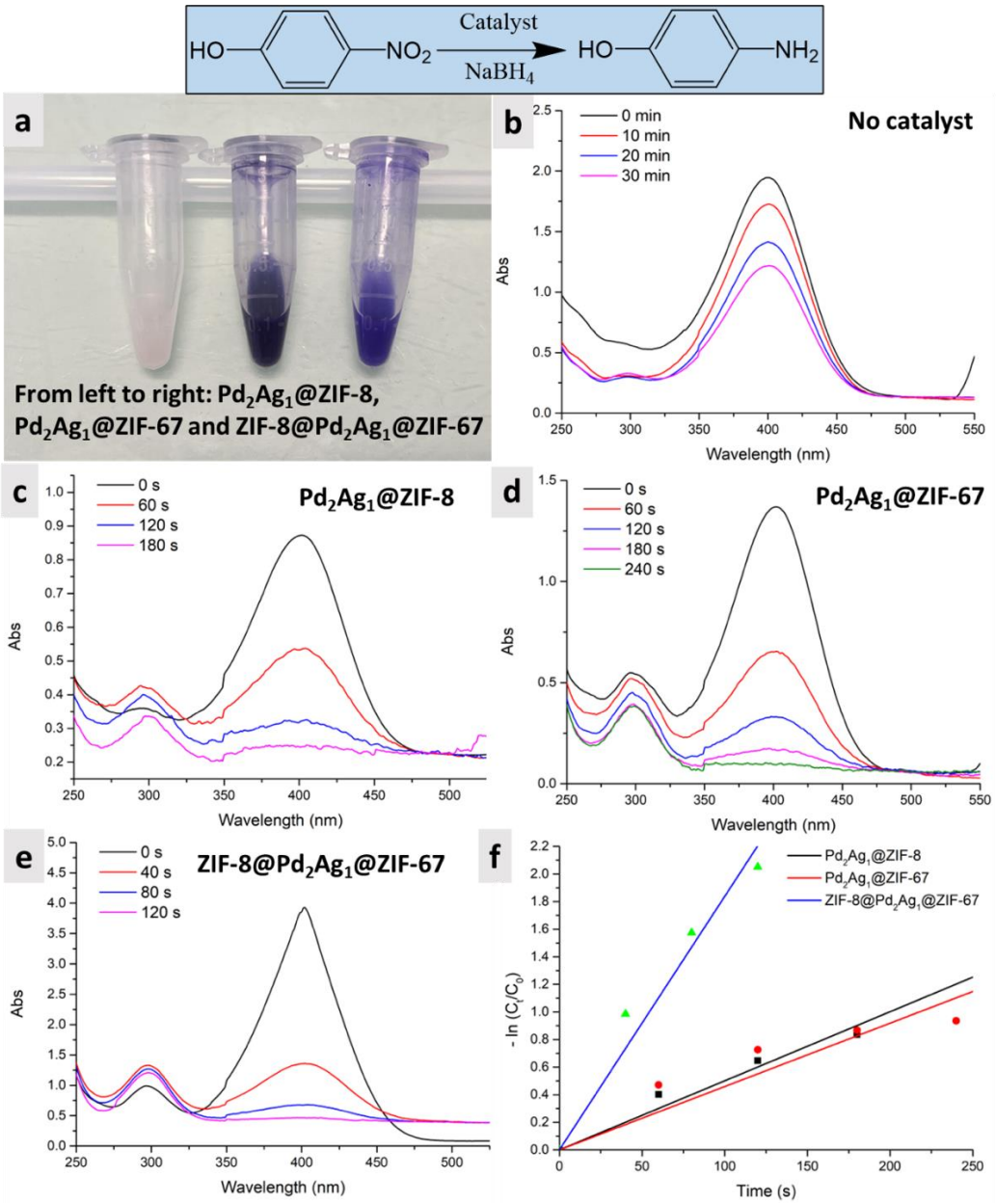

Figure 7. Time-dependent UV-vis. spectra for the reduction of 4-NP at 22 °C. (a) Catalyst images, (b) without catalyst, (c) in presence of Pd_2Ag_1@ZIF-8, (d) in presence of Pd_2Ag_1@ZIF-67, (e) in presence of ZIF-8@Pd_2Ag_1@ZIF-67 and (f) plot of $\ln(C_t/C_0)$ vs. the time of reaction of the catalytic reaction. C_t and C_0 are the concentrations of 4-NP at the time t and the time 0, respectively.

Conclusion

A new mode of MOF encapsulation of NP catalyst has been probed with the composed ZIF-8@ZIF-67 structure, and the large decrease of the BET surface after encapsulation showed the success of this attempt. Thus, Pd–Ag alloy NPs of various metal compositions have been easily and successfully stabilized in the ZIF-8@ZIF-67 structure, leading to stable monodisperse NPs. The characterization techniques

confirmed the core-shell structure, affording a highly effective and recyclable system for H_2 production from FA dehydrogenation. In addition, the optimized synergy for AgPd in MOFs toward catalytic hydrogen generation from FA under light irradiation involves Ag to Pd plasmonic "hot" electron transfer provoking electronic enrichment at the Pd catalytic sites. As a result, a large acceleration of the reaction was obtained under visible-light illumination compared to that in the dark. The superiority of the confinement provided by the ZIF sandwich compared to only ZIF-8 or ZIF-67 support is found in the dark, but it is even more marked under light illumination, emphasizing the boosted advantage of using in the same time double ZIF and visible light comprising the plasmonic region. Electronically promoted Pd sites by the LSPR effect of Ag combined with electronic enrichment of Pd due to favorable SF coordination facilitated the key steps of FA dehydrogenation, improving the catalytic performance. Finally, a new detailed mechanism of FA dehydrogenation is proposed, explaining both the SF and light effect confirmed by XPS results. The new sandwiched NP confinement constraints appear to induce additional stereo-electronic synergies to those optimized here in the alloy, particularly with visible light. All these advances should improve the required parameters towards efficient H_2 evolution from abundant and cheap FA, a major biomass product.

In addition, the possible extension to other reactions of the new improved support using the ZIF-8@Pd_2Ag_1@ZIF-67 catalyst has been confirmed with the model 4-nitrophenol reduction reaction, showing the superiority of ZIF-8@Pd_2Ag_1@ZIF-67 compared to Pd_2Ag_1@ZIF-8 and Pd_2Ag_1@ZIF-67.

Declaration of Competing Interest

The authors declare that they have no known competing financial interests.

Acknowledgments

Financial support from the China Scholarship Council (CSC, PhD grant to Yue Liu), the MAT2017-88752-R Retos Project from the Ministerio de Economía, Industria y Competitividad, gobierno de España (Dr Sergio Moya), the Universities of Bordeaux and Rennes and the Centre National de la Recherche Scientifique (CNRS) is gratefully acknowledged.

Dedication

This article is dedicated to our distinguished colleague Professor Jean-Marie Basset on the occasion of his 80th birthday.

ASSOCIATED CONTENT

Supporting Information available. [Materials and methods and catalyst characterization (ICP-AES, X-ray diffraction, N_2 adsorption-desorption isotherms and DFT pore distribution) and catalysis experimental data (Arrhenius plots, UV-Vis., temperature change under irradiation, comparison of TOFs with literature).]

References

(1) He, T.; Pachfule, P.; Wu, H.; Xu, Q.; Chen, P. Hydrogen Carriers. *Nat. Rev. Mater.* **2016**, *1* (12), 1–17. DOI: 10.1038/natrevmats.2016.59.

(2) Zhu, Q.-L.; Xu, Q. Liquid Organic and Inorganic Chemical Hydrides for High-Capacity Hydrogen Storage. *Energy Environ. Sci.* **2015**, *8* (2), 478–512. DOI: 10.1039/C4EE03690E.

(3) Wang, C.; Wang, Q.; Fu, F.; Astruc, D. Hydrogen Generation upon Nanocatalyzed Hydrolysis of Hydrogen-Rich Boron Derivatives: Recent Developments. *Acc. Chem. Res.* **2020**, *53* (10), 2483–2493. DOI: 10.1021/acs.accounts.0c00525.

(4) Cipriani, G.; Di Dio, V.; Genduso, F.; La Cascia, D.; Liga, R.; Miceli, R.; Ricco Galluzzo, G. Perspective on Hydrogen Energy Carrier and Its Automotive Applications. *Int. J. Hydrog. Energ.* **2014**, *39* (16), 8482–8494. DOI: 10.1016/j.ijhydene.2014.03.174.

(5) Jiang, H.-L.; Singh, S. K.; Yan, J.-M.; Zhang, X.-B.; Xu, Q. Liquid-Phase Chemical Hydrogen Storage: Catalytic Hydrogen Generation under Ambient Conditions. *ChemSusChem* **2010**, *3* (5), 541–549. DOI: 10.1002/cssc.201000023.

(6) Bulushev, D. A.; Ross, J. R. H. Towards Sustainable Production of Formic Acid. *ChemSusChem* **2018**, *11* (5), 821–836. DOI: cssc.201702075.

(7) Mellmann, D.; Sponholz, P.; Junge, H.; Beller, M. Formic Acid as a Hydrogen Storage Material – Development of Homogeneous Catalysts for Selective Hydrogen Release. *Chem. Soc. Rev.* **2016**, *45* (14), 3954–3988. DOI: 10.1039/C5CS00618J.

(8) Sponholz, P.; Mellmann, D.; Junge, H.; Beller, M. Towards a Practical Setup for Hydrogen Production from Formic Acid. *ChemSusChem* **2013**, *6* (7), 1172–1176. DOI: 10.1002/cssc.201300186.

(9) Jiang, Y.; Fan, X.; Xiao, X.; Qin, T.; Zhang, L.; Jiang, F.; Li, M.; Li, S.; Ge, H.; Chen, L. Novel AgPd Hollow Spheres Anchored on Graphene as an Efficient Catalyst for Dehydrogenation of Formic Acid at Room Temperature. *J. Mater. Chem. A.* **2016**, *4* (2), 657–666. DOI: 10.1039/C5TA09159D.

(10) Bielinski, E. A.; Lagaditis, P. O.; Zhang, Y.; Mercado, B. Q.; Würtele, C.; Bernskoetter, W. H.; Hazari, N.; Schneider, S. Lewis Acid-Assisted Formic Acid Dehydrogenation Using a Pincer-Supported Iron Catalyst. *J. Am. Chem. Soc.* **2014**, *136* (29), 10234–10237. DOI: 10.1021/ja505241x.

(11) Bi, Q.-Y.; Du, X.-L.; Liu, Y.-M.; Cao, Y.; He, H.-Y.; Fan, K.-N. Efficient Subnanometric Gold-Catalyzed Hydrogen Generation via Formic Acid Decomposition under Ambient Conditions.

J. Am. Chem. Soc. **2012**, *134* (21), 8926–8933. DOI: 10.1021/ja301696e.

(12) Younas, M.; Rezakazemi, M.; Arbab, M. S.; Shah, J.; Rehman, W. U. Green Hydrogen Storage and Delivery: Utilizing Highly Active Homogeneous and Heterogeneous Catalysts for Formic Acid Dehydrogenation. *Int. J. Hydrog. Energ.* **2022**, *47* (22), 11694–11724. DOI: 10.1016/j.ijhydene.2022.01.184.

(13) Li, S.-J.; Zhou, Y.-T.; Kang, X.; Liu, D.-X.; Gu, L.; Zhang, Q.-H.; Yan, J.-M.; Jiang, Q. A Simple and Effective Principle for a Rational Design of Heterogeneous Catalysts for Dehydrogenation of Formic Acid. *Adv. Mater.* **2019**, *31* (15), 1806781. DOI: 10.1002/adma.201806781.

(14) Ping, Y.; Yan, J.-M.; Wang, Z.-L.; Wang, H.-L.; Jiang, Q. Ag 0.1 -Pd 0.9 /RGO: An Efficient Catalyst for Hydrogen Generation from Formic Acid /Sodium Formate. *J. Mater. Chem. A.* **2013**, *1* (39), 12188–12191. DOI: 10.1039/C3TA12724A.

(15) Zhou, X.; Huang, Y.; Liu, C.; Liao, J.; Lu, T.; Xing, W. Available Hydrogen from Formic Acid Decomposed by Rare Earth Elements Promoted Pd-Au/C Catalysts at Low Temperature. *ChemSusChem* **2010**, *3* (12), 1379–1382. DOI: 10.1002/cssc.201000199.

(16) Wang, Z.-L.; Yan, J.-M.; Wang, H.-L.; Ping, Y.; Jiang, Q. Au@Pd Core–Shell Nanoclusters Growing on Nitrogen-Doped Mildly Reduced Graphene Oxide with Enhanced Catalytic Performance for Hydrogen Generation from Formic Acid. *J. Mater. Chem. A.* **2013**, *1* (41), 12721–12725. DOI: 10.1039/C3TA12531A.

(17) Metin, Ö.; Sun, X.; Sun, S. Monodisperse Gold–Palladium Alloy Nanoparticles and Their Composition-Controlled Catalysis in Formic Acid Dehydrogenation under Mild Conditions. *Nanoscale* **2013**, *5* (3), 910–912. DOI: 10.1039/C2NR33637E.

(18) Tedsree, K.; Li, T.; Jones, S.; Chan, C. W. A.; Yu, K. M. K.; Bagot, P. A. J.; Marquis, E. A.; Smith, G. D. W.; Tsang, S. C. E. Hydrogen Production from Formic Acid Decomposition at Room Temperature Using a Ag–Pd Core–Shell Nanocatalyst. *Nat. Nanotech.* **2011**, *6* (5), 302–307. DOI: 10.1038/nnano.2011.42.

(19) Mori, K.; Dojo, M.; Yamashita, H. Pd and Pd–Ag Nanoparticles within a Macroreticular Basic Resin: An Efficient Catalyst for Hydrogen Production from Formic Acid Decomposition. *ACS Catal.* **2013**, *3* (6), 1114–1119. DOI: 10.1021/cs400148n.

(20) Zhang, S.; Metin, Ö.; Su, D.; Sun, S. Monodisperse AgPd Alloy Nanoparticles and Their Superior Catalysis for the Dehydrogenation of Formic Acid. *Angew. Chem. Int. Ed.* **2013**, *52* (13), 3681–3684. DOI: 10.1002/anie.201300276.

(21) Xu, F.; Liu, X. "On–Off" Control for On-Demand Hydrogen Production from the Dehydrogenation of Formic Acid. *ACS Catal.* **2021**, *11* (22), 13913–13920. DOI: 10.1021/acscatal.1c03923.

(22) Hausoul, P. J. C.; Broicher, C.; Vegliante, R.; Göb, C.; Palkovits, R. Solid Molecular Phosphine Catalysts for Formic Acid Decomposition in the Biorefinery. *Angew. Chem. Int. Ed.* **2016**, *55* (18), 5597–5601. DOI: 10.1002/anie.201510681.

(23) Yu, W.-Y.; Mullen, G. M.; Flaherty, D. W.; Mullins, C. B. Selective Hydrogen Production from Formic Acid Decomposition on Pd–Au Bimetallic Surfaces. *J. Am. Chem. Soc.* **2014**, *136* (31), 11070–11078. DOI: 10.1021/ja505192v.

(24) Boddien, A.; Mellmann, D.; Gärtner, F.; Jackstell, R.; Junge, H.; Dyson, P. J.; Laurenczy, G.; Ludwig, R.; Beller, M. Efficient Dehydrogenation of Formic Acid Using an Iron Catalyst. *Science* **2011**, *333* (6050), 1733–1736. DOI: 10.1126/science.1206613.

(25) Barrett, S. M.; Slattery, S. A.; Miller, A. J. M. Photochemical Formic Acid Dehydrogenation by Iridium Complexes: Understanding Mechanism and Overcoming Deactivation. *ACS Catal.* **2015**, *5* (11), 6320–6327. DOI: 10.1021/acscatal.5b01995.

(26) Liu, H.; Yu, Y.; Yang, W.; Lei, W.; Gao, M.; Guo, S. High-Density Defects on PdAg Nanowire Networks as Catalytic Hot Spots for Efficient Dehydrogenation of Formic Acid and Reduction of Nitrate. *Nanoscale* **2017**, *9* (27), 9305–9309. DOI: 10.1039/C7NR03734A.

(27) Liu, H.; Guo, Y.; Yu, Y.; Yang, W.; Shen, M.; Liu, X.; Geng, S.; Li, J.; Yu, C.; Yin, Z.; Li, H. Surface Pd-Rich PdAg Nanowires as Highly Efficient Catalysts for Dehydrogenation of Formic Acid and Subsequent Hydrogenation of Adiponitrile. *J. Mater. Chem. A.* **2018**, *6* (36), 17323–17328. DOI: 10.1039/C8TA06513F.

(28) Liu, H.; Liu, X.; Yu, Y.; Yang, W.; Li, J.; Feng, M.; Li, H. Bifunctional Networked Ag/AgPd Core/Shell Nanowires for the Highly Efficient Dehydrogenation of Formic Acid and Subsequent Reduction of Nitrate and Nitrite in Water. *J. Mater. Chem. A.* **2018**, *6* (11), 4611–4616. DOI: 10.1039/C8TA00600H.

(29) Xiao, L.; Jun, Y.-S.; Wu, B.; Liu, D.; T Chuong, T.; Fan, J.; D. Stucky, G. Carbon Nitride Supported AgPd Alloy Nanocatalysts for Dehydrogenation of Formic Acid under Visible Light. *J. Mater. Chem. A.* **2017**, *5* (14), 6382–6387. DOI: 10.1039/C7TA01039G.

(30) Kuehnel, M. F.; Wakerley, D. W.; Orchard, K. L.; Reisner, E. Photocatalytic Formic Acid Conversion on CdS Nanocrystals with Controllable Selectivity for H2 or CO. *Angew. Chem. Int. Ed.* **2015**, *54* (33), 9627–9631. DOI: 10.1002/anie.201502773.

(31) Mascaretti, L.; Dutta, A.; Kment, Š.; Shalaev, V. M.; Boltasseva, A.; Zbořil, R.; Naldoni, A. Plasmon-Enhanced Photoelectrochemical Water Splitting for Efficient Renewable Energy Storage. *Adv. Mater.* **2019**, *31* (31), 1805513. DOI: 10.1002/adma.201805513.

(32) Daniel, M.-C.; Astruc, D. Gold Nanoparticles: Assembly, Supramolecular Chemistry, Quantum-Size-Related Properties, and Applications toward Biology, Catalysis, and Nanotechnology. *Chem. Rev.* **2004**, *104* (1), 293–346. DOI: 10.1021/cr030698+.

(33) Gellé, A.; Jin, T.; de la Garza, L.; Price, G. D.; Besteiro, L. V.; Moores, A. Applications of Plasmon-Enhanced Nanocatalysis to Organic Transformations. *Chem. Rev.* **2020**, *120* (2), 986–1041. DOI: 10.1021/acs.chemrev.9b00187.

(34) Linic, S.; Christopher, P.; Ingram, D. B. Plasmonic-Metal Nanostructures for Efficient Conversion of Solar to Chemical Energy. *Nat. Mater.* **2011**, *10* (12), 911–921. DOI: 10.1038/nmat3151.

(35) Wang, C.; Astruc, D. Nanogold Plasmonic Photocatalysis for Organic Synthesis and Clean Energy Conversion. *Chem. Soc. Rev.* **2014**, *43* (20), 7188–7216. DOI: 10.1039/C4CS00145A.

(36) Wang, Q.; Astruc, D. State of the Art and Prospects in Metal–Organic Framework (MOF)-Based and MOF-Derived Nanocatalysis. *Chem. Rev.* **2020**, *120* (2), 1438–1511. DOI: 10.1021/acs.chemrev.9b00223.

(37) Hattori, M.; Shimamoto, D.; Ago, H.; Tsuji, M. AgPd@Pd/TiO2 Nanocatalyst Synthesis by Microwave Heating in Aqueous Solution for Efficient Hydrogen Production from Formic Acid. *J. Mater. Chem. A.* **2015**, *3* (20), 10666–10670. DOI: 10.1039/C5TA01434D.

(38) Zhao, M.; Yuan, K.; Wang, Y.; Li, G.; Guo, J.; Gu, L.; Hu, W.; Zhao, H.; Tang, Z. Metal–Organic Frameworks as Selectivity Regulators for Hydrogenation Reactions. *Nature* **2016**, *539* (7627), 76–80. DOI: 10.1038/nature19763.

(39) Pan, Y.; Sun, K.; Liu, S.; Cao, X.; Wu, K.; Cheong, W.-C.; Chen, Z.; Wang, Y.; Li, Y.; Liu, Y.; Wang, D.; Peng, Q.; Chen, C.; Li, Y. Core–Shell ZIF-8@ZIF-67-Derived CoP Nanoparticle-Embedded N-Doped Carbon Nanotube Hollow Polyhedron for Efficient Overall Water Splitting. *J. Am. Chem. Soc.* **2018**, *140* (7), 2610–2618. DOI: 10.1021/jacs.7b12420.

(40) Yang, J.; Zhang, F.; Lu, H.; Hong, X.; Jiang, H.; Wu, Y.; Li, Y. Hollow Zn/Co ZIF Particles Derived from Core–Shell ZIF-67@ZIF-8 as Selective Catalyst for the Semi-Hydrogenation of Acetylene. *Angew. Chem.* Int. Ed. **2015**, *54*, 10889–10893. DOI: 1002/anie.201504242.

(41) Panchariya, D. K.; Rai, R. K.; Anil Kumar, E.; Singh, S. K. Core–Shell Zeolitic Imidazolate Frameworks for Enhanced Hydrogen Storage. *ACS Omega* **2018**, *3* (1), 167–175. DOI: 10.1021/acsomega.7b01693.

(42) Yun, Y.; Sheng, H.; Bao, K.; Xu, L.; Zhang, Y.; Astruc, D.; Zhu, M. Design and Remarkable Efficiency of the Robust Sandwich Cluster Composite Nanocatalysts ZIF-8@Au25@ZIF-67. *J. Am. Chem. Soc.* **2020**, *142* (9), 4126–4130. DOI: 10.1021/jacs.0c00378.

(43) Wan, M.; Zhang, X.; Li, M.; Chen, B.; Yin, J.; Jin, H.; Lin, L.; Chen, C.; Zhang, N. Hollow Pd/MOF Nanosphere with Double Shells as Multifunctional Catalyst for Hydrogenation Reaction. *Small* **2017**, *13* (38), 1701395. DOI: 10.1002/smll.201701395.

(44) Zhang, A.; Xia, J.; Yao, Q.; Lu, Z.-H. Pd–WOx Heterostructures Immobilized by MOFs-Derived Carbon Cage for Formic Acid Dehydrogenation. *Appl. Catal. B environ.* **2022**, *309*, 121278. DOI: 10.1016/j.apcatb.2022.121278.

(45) Michaud, P.; Astruc, D.; Ammeter, J. H. Electron-Transfer Pathways in the Reduction of D6 and D7 Organoiron Cations by Lithium Tetrahydroaluminate and Sodium Tetrahydroborate. *J. Am. Chem. Soc.* **1982**, *104* (13), 3755–3757. DOI: 10.1021/ja00377a051.

(46) Lü, B.; Qi, W.; Luo, M.; Liu, Q.; Guo, L. Fischer–Tropsch Synthesis: ZIF-8@ZIF-67-Derived Cobalt Nanoparticle-Embedded Nanocage Catalysts. *Ind. Eng. Chem. Res.* **2020**, *59* (27), 12352–12359. DOI: 10.1021/acs.iecr.0c00971.

(47) Liu, H.; Liu, X.; Yang, W.; Shen, M.; Geng, S.; Yu, C.; Shen, B.; Yu, Y. Photocatalytic Dehydrogenation of Formic Acid Promoted by a Superior PdAg@g-C 3 N 4 Mott–Schottky Heterojunction. *J. Mater. Chem. A.* **2019**, *7* (5), 2022–2026. DOI: 10.1039/C8TA11172C.

(48) Aijaz, A.; Karkamkar, A.; Choi, Y. J.; Tsumori, N.; Rönnebro, E.; Autrey, T.; Shioyama, H.; Xu, Q. Immobilizing Highly Catalytically Active Pt Nanoparticles inside the Pores of Metal–Organic Framework: A Double Solvents Approach. *J. Am. Chem. Soc.* **2012**, *134* (34), 13926–13929. DOI: 10.1021/ja3043905.

(49) Zhu, Q.-L.; Li, J.; Xu, Q. Immobilizing Metal Nanoparticles to Metal–Organic Frameworks with Size and Location Control for Optimizing Catalytic Performance. *J. Am. Chem. Soc.* **2013**, *135* (28), 10210–10213. DOI: 10.1021/ja403330m.

(50) Jiang, H.-L.; Akita, T.; Ishida, T.; Haruta, M.; Xu, Q. Synergistic Catalysis of Au@Ag Core−Shell Nanoparticles Stabilized on Metal−Organic Framework. *J. Am. Chem. Soc.* **2011**, *133* (5), 1304–1306. DOI: 10.1021/ja1099006.

(51) Gu, A.; Chen, J.; Gao, Q.; Khan, M. M.; Wang, P.; Jiao, Y.; Zhang, Z.; Liu, Y.; Yang, Y. The Preparation of Ag/ZIF-8@ZIF-67 Core-Shell Composites as Excellent Catalyst for Degradation of the Nitroaromatic Compounds. *Appl. Surf. Sci.* **2020**, *516*, 146160. DOI: 10.1016/j.apsusc.2020.146160.

(52) Tang, J.; Salunkhe, R. R.; Liu, J.; Torad, N. L.; Imura, M.; Furukawa, S.; Yamauchi, Y. Thermal Conversion of Core–Shell Metal–Organic Frameworks: A New Method for

Selectively Functionalized Nanoporous Hybrid Carbon. *J. Am. Chem. Soc.* **2015**, *137* (4), 1572–1580. DOI: 10.1021/ja511539a.

(53) Dai, H.; Xia, B.; Wen, L.; Du, C.; Su, J.; Luo, W.; Cheng, G. Synergistic Catalysis of AgPd@ZIF-8 on Dehydrogenation of Formic Acid. *Appl. Catal. B environ.* **2015**, *165*, 57–62. DOI: 10.1016/j.apcatb.2014.09.065.

(54) Sun, X.; Li, F.; Wang, Z.; An, H.; Xue, W.; Wang, Y. AgPd Nanoparticles Anchored on TiO2 Derived from a Titanium Metal–Organic Framework for Efficient Dehydrogenation of Formic Acid. *ChemCatChem* **2022**, *14* (2), e202101528. DOI: 10.1002/cctc.202101528.

(55) Wen, M.; Mori, K.; Kuwahara, Y.; Yamashita, H. Plasmonic Au@Pd Nanoparticles Supported on a Basic Metal–Organic Framework: Synergic Boosting of H2 Production from Formic Acid. *ACS Energy Lett.* **2017**, *2* (1), 1–7. DOI: 10.1021/acsenergylett.6b00558.

(56) Hong, D.; Sharma, A.; Jiang, D.; Stellino, E.; Ishiyama, T.; Postorino, P.; Placidi, E.; Kon, Y.; Koga, K. Laser Ablation Nanoarchitectonics of Au–Cu Alloys Deposited on TiO2 Photocatalyst Films for Switchable Hydrogen Evolution from Formic Acid Dehydrogenation. *ACS Omega* **2022**, *7* (35), 31260–31270. DOI: 10.1021/acsomega.2c03509.

(57) Issa Hamoud, H.; Damacet, P.; Fan, D.; Assaad, N.; Lebedev, O. I.; Krystianiak, A.; Gouda, A.; Heintz, O.; Daturi, M.; Maurin, G.; Hmadeh, M.; El-Roz, M. Selective Photocatalytic Dehydrogenation of Formic Acid by an In Situ-Restructured Copper-Postmetalated Metal–Organic Framework under Visible Light. *J. Am. Chem. Soc.* **2022**, *144* (36), 16433–16446. DOI: 10.1021/jacs.2c04905.

(58) Verma, P.; Kuwahara, Y.; Mori, K.; Yamashita, H. Pd/Ag and Pd/Au Bimetallic Nanocatalysts on Mesoporous Silica for Plasmon-Mediated Enhanced Catalytic Activity under Visible Light Irradiation. *J. Mater. Chem. A.* **2016**, *4* (26), 10142–10150. DOI: 10.1039/C6TA01664B.

(59) Kang, H.; Buchman, J. T.; Rodriguez, R. S.; Ring, H. L.; He, J.; Bantz, K. C.; Haynes, C. L. Stabilization of Silver and Gold Nanoparticles: Preservation and Improvement of Plasmonic Functionalities. *Chem. Rev.* **2019**, *119* (1), 664–699. DOI: 10.1021/acs.chemrev.8b00341.

(60) Tong, F.; Liang, X.; Wang, Z.; Liu, Y.; Wang, P.; Cheng, H.; Dai, Y.; Zheng, Z.; Huang, B. Probing the Mechanism of Plasmon-Enhanced Ammonia Borane Methanolysis on a CuAg Alloy at a Single-Particle Level. *ACS Catal.* **2021**, *11* (17), 10814–10823. DOI: 10.1021/acscatal.1c02857.

(61) Xu, P.; Lu, W.; Zhang, J.; Zhang, L. Efficient Hydrolysis of Ammonia Borane for Hydrogen Evolution Catalyzed by Plasmonic Ag@Pd Core–Shell Nanocubes. *ACS Sustainable Chem. Eng.* **2020**, *8* (33), 12366–12377. DOI: 10.1021/acssuschemeng.0c02276.

(62) Kang, N.; Shen, R.; Li, B.; Fu, F.; Espuche, B.; Moya, S.; Salmon, L.; Pozzo, J.-L.; Astruc, D. Dramatic Acceleration by Visible Light and Mechanism of AuPd@ZIF-8-Catalyzed Ammonia Borane Methanolysis for Efficient Hydrogen Production. *J. Mater. Chem. A.* **2023**, *11*, 5245-5256. DOI: 10.1039/D2TA08396E.

(63) Kang, N.; Wei, X.; Shen, R.; Li, B.; Cal, E. G.; Moya, S.; Salmon, L.; Wang, C.; Coy, E.; Berlande, M.; Pozzo, J.-L.; Astruc, D. Fast Au-Ni@ZIF-8-Catalyzed Ammonia Borane Hydrolysis Boosted by Dramatic Volcano-Type Synergy and Plasmonic Acceleration. *Appl. Catal. B environ.* **2023**, *320*, 121957. DOI: 10.1016/j.apcatb.2022.121957.

(64) Twilton, J.; Le, C. (Chip); Zhang, P.; Shaw, M. H.; Evans, R. W.; MacMillan, D. W. C. The Merger of Transition Metal and Photocatalysis. *Nat. Rev. Chem.* **2017**, *1* (7), 1–19. DOI: 10.1038/s41570-017-0052.

(65) Park, Y.; Tian, L.; Kim, S.; Pabst, T. P.; Kim, J.; Scholes, G. D.; Chirik, P. J. Visible-Light-Driven, Iridium-Catalyzed Hydrogen Atom Transfer: Mechanistic Studies, Identification of Intermediates, and Catalyst Improvements. *JACS Au* **2022**, *2* (2), 407–418. DOI: 10.1021/jacsau.1c00460.

(66) Astruc, D. *Organometallic Chemistry and Catalysis*; Springer: Berlin, Heidelberg, 2007; pp 81–107. DOI: 10.1007/978-3-540-46129-6_5.

(67) Astruc, D. Palladium Catalysis Using Dendrimers: Molecular Catalysts versus Nanoparticles. *Tetrahedron Asym.* **2010**, *21* (9-10), 1041-1054. DOI: 10.1016/j.tetasy.2010.04.062.

(68) Wang, F.; Li, C.; Chen, H.; Jiang, R.; Sun, L.-D.; Li, Q.; Wang, J.; Yu, J. C.; Yan, C.-H. Plasmonic Harvesting of Light Energy for Suzuki Coupling Reactions. *J. Am. Chem. Soc.* **2013**, *135* (15), 5588–5601. DOI: 10.1021/ja310501y.

(69) Sarina, S.; Zhu, H.; Jaatinen, E.; Xiao, Q.; Liu, H.; Jia, J.; Chen, C.; Zhao, J. Enhancing Catalytic Performance of Palladium in Gold and Palladium Alloy Nanoparticles for Organic Synthesis Reactions through Visible Light Irradiation at Ambient Temperatures. *J. Am. Chem. Soc.* **2013**, *135* (15), 5793–5801. DOI: 10.1021/ja400527a.

(70) Pradhan, N.; Pal, A.; Pal, T. Silver nanoparticle catalyzed reduction of aromatic nitro compounds, *Colloids Surf.* **2002**, *96* (2-3), 247– 257. DOI 10.1016/S0927-7757(01)01040-8.

(71) Wunder, S.; Polzer, F.; Lu, Y.; Mei, Y.; Ballauff, M. Kinetic Analysis of Catalytic Reduction of 4-Nitrophenol by Metallic Nanoparticles Immobilized in Spherical Polyelectrolyte Brushes, *J. Phys. Chem. C* **2010**, *114* (19), 8814-8820. DOI 10.1021/jp101125j.

TOC

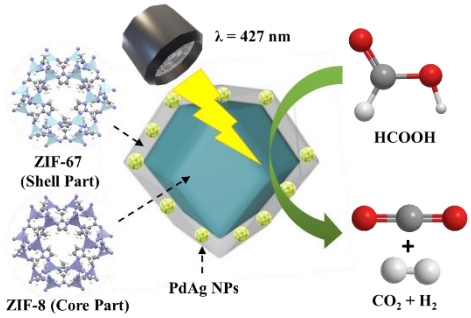

MOF support is easily improved with ZIF-8@ZIF-67-encapsulation of AgPd nanoalloys toward photocatalytic H_2 production from formic acid under visible-light illumination, optimized with the nanocatalyst ZIF-8@Pd_2Ag_1@ZIF-67.